

Generator-based Graph Generation via Heat Diffusion

Anthony Stephenson^{1,2} Ian Gallagher³ Christopher Nemeth¹

Abstract

Graph generative modelling has become an essential task due to the wide range of applications in chemistry, biology, social networks, and knowledge representation. In this work, we propose a novel framework for generating graphs by adapting the Generator Matching (Holderrieth et al., 2024) paradigm to graph-structured data. We leverage the graph Laplacian and its associated heat kernel to define a continuous-time diffusion on each graph. The Laplacian serves as the infinitesimal generator of this diffusion, and its heat kernel provides a family of conditional perturbations of the initial graph. A neural network is trained to match this generator by minimising a Bregman divergence between the true generator and a learnable surrogate. Once trained, the surrogate generator is used to simulate a time-reversed diffusion process to sample new graph structures. Our framework unifies and generalises existing diffusion-based graph generative models, injecting domain-specific inductive bias via the Laplacian, while retaining the flexibility of neural approximators. Experimental studies demonstrate that our approach captures structural properties of real and synthetic graphs effectively.

1. Introduction

Graph generative modelling has emerged as a critical research area due to the broad applicability of graphs in representing complex systems such as molecular structures (Sylvester, 1878; De Cao & Kipf, 2018), social networks (Nettleton, 2013), and knowledge graphs (Schneider, 1973; Ji et al., 2021). The goal in graph generation is to learn the

¹MARS: Mathematics for AI in Real-world Systems, School of Mathematical Sciences Lancaster University Lancaster, LA1 4YF, UK. ²Department of Mathematics, University of Bristol, Bristol BS8 1UG, UK. ³School of Mathematics and Statistics, University of Melbourne, Parkville, VIC, 3010, Australia.. Correspondence to: Anthony Stephenson <ant.stephenson@bristol.ac.uk>, Ian Gallagher <ian.gallagher@unimelb.edu.au>, Christopher Nemeth <c.nemeth@lancaster.ac.uk>.

underlying distribution of a collection of observed graphs and generate new samples that exhibit similar structural properties. Applications range from de novo molecule design in chemistry (Brown et al., 2019) to synthetic network construction for privacy-preserving data sharing (Fu et al., 2023). However, *structured* data like graphs pose unique challenges for generative models, owing to their discrete combinatorial nature and the permutation symmetries among node labels.

Early approaches to graph generation include graph-structured variational autoencoders (Kipf & Welling, 2016), autoregressive models (You et al., 2018), and generative adversarial networks (Wang et al., 2018). While these methods achieved partial success, they often struggled to capture higher-order dependencies or to enforce fundamental invariances such as permutation symmetry. More recently, score-based generative models—also known as diffusion models—have demonstrated remarkable performance in continuous domains such as images by progressively transforming noise into data via a forward diffusion and learned reverse process (Song et al., 2020). This success has spurred increasing interest in adapting diffusion models to graph-structured data, giving rise to *graph diffusion models*. Existing approaches typically operate on adjacency matrices or node and edge features, and have shown promising results in tasks such as molecule generation and network completion (Vignac et al., 2022; Yang et al., 2023). Notably, some recent methods formulate permutation-invariant stochastic differential equations that jointly diffuse node and edge attributes (Jo et al., 2022), while others apply diffusion in a continuous latent space obtained via graph autoencoders. Despite these advances, defining principled and effective diffusion processes *directly* on discrete graph structures remains challenging, motivating the development of more general, generator-centric frameworks.

Contributions. In this paper we propose *Generator-based Graph Generation* (G^3), a generator-matching approach to graph generative modelling in which we (a) choose a principled, topology-aware *forward* noising mechanism given by Laplacian heat diffusion on a matrix representation of a graph, (b) exploit its closed-form infinitesimal generator to define an explicit learning target, and (c) train a neural surrogate generator from forward-diffused samples. At sampling

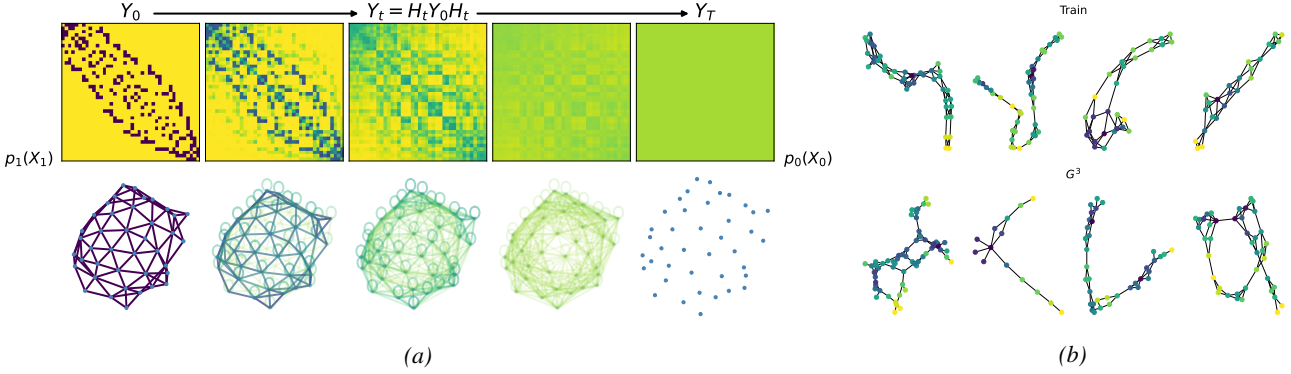


Figure 1. (a) shows the effect of the symmetric heat diffusion process on a graph (bottom row) and its adjacency (top) as t increases and the probability mass is spread over all possible edges. Colours indicate this value, with yellow and purple the respective extremes of the interval $[0, 1]$ and edge transparency governed by the same quantity. (b) shows a series of randomly drawn graphs from the (training) subset of the Enzyme dataset (top) and output graphs from G^3 (bottom). Node colouring reflects Forman-Ricci curvature (Forman, 2003) at that node.

time, we integrate the learned reverse-time ODE from a simple, permutation-symmetric base distribution to obtain a real-valued graph matrix, which is then mapped to a discrete adjacency matrix. Figure 1a illustrates the forward-reverse behaviour of the G^3 framework.

2. Background

Continuous-time generative models can be formulated in terms of deterministic or stochastic dynamics that transform samples from a simple reference distribution into samples from a complex data distribution. One of the most popular approaches for learning such dynamics is *flow matching*, and its extension *generator matching*. In addition to reviewing these paradigms in a general setting, we also establish the graph-theoretic preliminaries—matrix representations and Laplacian heat diffusion—that underpin our G^3 framework introduced in Section 3.

2.1. Graph Matrix Representations

We consider undirected simple graphs $G = (V, E)$ with $n = |V|$ nodes $V = \{1, \dots, n\}$ and edge set $E \subseteq \{\{i, j\} : i, j \in V, i \neq j\}$. The adjacency matrix $A \in \{0, 1\}^{n \times n}$ represents the connectivity in the graph where $A_{ij} = 1$ iff $\{i, j\} \in E$, and $A_{ii} = 0$ otherwise. The degree matrix $D = \text{diag}(d_1, \dots, d_n)$ is the diagonal matrix of node degrees $d_i = \sum_{j=1}^n A_{ij}$.

The combinatorial Laplacian $L = D - A$ is a symmetric positive semidefinite matrix that describes heat diffusion on an undirected graph. For a connected graph, the Laplacian has eigenvalue 0 with multiplicity 1 with the all-one eigenvector $\mathbf{1}$, $L\mathbf{1} = 0$.

Other versions of the Laplacian matrix normalise the graph structure in different ways, e.g., the random-walk Laplacian

$L_{\text{rw}} = I - D^{-1}A$. The following methodology applies to alternative Laplacian matrices but, by default, results refer to the combinatorial Laplacian unless stated otherwise.

2.2. Heat Equation on Graphs and the Heat Kernel

We consider heat diffusion on an undirected graph and introduce its solution, known as the *graph heat kernel*. This construction provides a notion of diffusion on graphs that will be utilised in our generative framework.

Definition 2.1 (Heat equation on a graph). Let $G = (V, E)$ be an undirected graph with $n = |V|$ nodes, graph Laplacian $L \in \mathbb{R}^{n \times n}$ and heat kernel

$$H_s := e^{-sL}, \quad s \geq 0. \quad (1)$$

Given an initial matrix-valued graph representation $Y_0 \in \mathbb{R}^{n \times n}$ (e.g. $Y_0 = A$ the adjacency matrix), define the *symmetric heat diffusion* by

$$Y_s := H_s Y_0 H_s, \quad s \geq 0. \quad (2)$$

Since $\frac{d}{ds} H_s = -LH_s = -H_s L$, differentiating (2) yields the matrix-valued heat equation

$$\frac{d}{ds} Y_s = -LY_s - Y_s L, \quad Y_0 = A. \quad (3)$$

(See Proposition A.1 in Appendix A.1 for a proof.) As L is symmetric positive semidefinite, the operator $Y \mapsto LY + YL$ is dissipative, and (3) defines a stable linear diffusion on graph-derived matrices (see Lemmas A.2 and A.4 in Appendix A.2 and Figure 1a for an illustration). Intuitively, left and right multiplication by H_s smooths the structure encoded in Y_0 in a manner consistent with the graph topology.

Although (2) can be viewed via its associated semigroup and long-time limit, we defer that perspective to Section 3.1, where it directly motivates our generator-matching formulation and the choice of base distribution.

2.3. Flow Matching

Flow matching (Lipman et al., 2022) is a framework for generative modelling in which one learns a deterministic *flow* that transports probability mass from a single, often simple, initial distribution to a target distribution over a continuous state space $\mathcal{X} \subseteq \mathbb{R}^d$. The approach can be viewed as a deterministic analogue of diffusion-based generative modelling (Song et al., 2020), in which stochastic dynamics are replaced by ordinary differential equations (ODEs).

Vector fields and probability paths. Let p_{init} denote a reference distribution on \mathcal{X} (often a Gaussian or uniform distribution), and let p_{data} denote the target data distribution. A flow matching model introduces a time-dependent vector field $u : \mathcal{X} \times [0, 1] \rightarrow \mathcal{X}$ and defines trajectories $(X_t)_{t \in [0, 1]}$ via the ODE

$$\frac{d}{dt} X_t = u_t(X_t), \quad X_0 \sim p_{\text{init}}. \quad (4)$$

The solution of this ODE induces (under mild regularity conditions) a *flow map* $\psi_t : \mathcal{X} \rightarrow \mathcal{X}$, such that $X_t = \psi_t(X_0)$. The goal is to learn a vector field u for which the terminal distribution X_1 matches the target data distribution p_{data} .

Rather than directly specifying u through a likelihood or score function, flow matching begins by prescribing a *probability path* $(p_t)_{t \in [0, 1]}$ interpolating between p_{init} and p_{data} . A time-dependent vector field $u^* : \mathcal{X} \times [0, 1] \rightarrow \mathcal{X}$ is said to be *consistent* with this path if (p_t) satisfies the continuity equation

$$\partial_t p_t(x) + \nabla \cdot (p_t(x), u_t^*(x)) = 0, \quad t \in (0, 1). \quad (5)$$

Surrogate vector field and objective. A neural vector field $u^\theta : \mathcal{X} \times [0, 1] \rightarrow \mathcal{X}$ is then trained to approximate u^* by minimising an expected discrepancy

$$\mathcal{L}_{\text{FM}}(\theta) = \mathbb{E}_{t \sim \text{Unif}, x \sim p_t} [D(u_t^*(x), u_t^\theta(x))], \quad (6)$$

where $D(\cdot, \cdot)$ is a *Bregman divergence*, typically the mean-squared error or KL divergence in practice.

Flow matching avoids numerical issues commonly associated with simulating stochastic differential equations (Song et al., 2020), admits flexible choices of probability paths, and can be implemented using standard ODE solvers at sampling time (Chen et al., 2018). However, the framework fundamentally operates at the level of *vector fields*, and does not explicitly constrain the learned dynamics to correspond to any underlying stochastic process or infinitesimal generator.

2.4. Generator Matching

Generator matching (Holderrieth et al., 2024) is a framework for learning continuous-time generative models in

which the focus shifts from matching vector fields to matching *infinitesimal generators* of Markov processes. Let $(X_t)_{t \in [0, 1]}$ be a (possibly *time-inhomogeneous*) continuous-time Markov process on a state space \mathcal{X} with (infinitesimal) generator \mathcal{J}_t . For sufficiently regular test functions $f : \mathcal{X} \rightarrow \mathbb{R}$ in the domain of \mathcal{J}_t , the generator is defined by

$$(\mathcal{J}_t f)(x) := \lim_{h \downarrow 0} \frac{\mathbb{E}[f(X_{t+h}) \mid X_t = x] - f(x)}{h}. \quad (7)$$

Semigroup and Kolmogorov equations. The generator viewpoint is tightly linked to the Kolmogorov equations describing how expectations and marginal laws evolve. In the *time-homogeneous* case (i.e. when $\mathcal{J}_t \equiv \mathcal{J}$ does not depend on t), the process induces a one-parameter Markov semigroup $(S_t)_{t \geq 0}$ acting on observables $f : \mathcal{X} \rightarrow \mathbb{R}$ by

$$(S_t f)(x) := \mathbb{E}[f(X_t) \mid X_0 = x], \quad t \geq 0,$$

and for $f \in \text{Dom}(\mathcal{J})$ this semigroup satisfies the Kolmogorov backward equation

$$\partial_t (S_t f) = \mathcal{J}(S_t f), \quad S_0 f = f.$$

(Equivalently, $\partial_t (S_t f) = S_t(\mathcal{J} f)$.) Dually, if p_t denotes the marginal law of X_t and \mathcal{J}^* is the adjoint of \mathcal{J} in the weak sense, then p_t evolves according to the forward (Fokker–Planck/master) equation

$$\partial_t p_t = \mathcal{J}^* p_t.$$

In the more general *time-inhomogeneous* setting one works with a family $(\mathcal{J}_t)_{t \in [0, 1]}$ and the corresponding evolution of $(S_t f)$ and (p_t) is still governed by these backward/forward equations with \mathcal{J} replaced by \mathcal{J}_t . This is precisely why generator matching is posed in terms of *generator actions*: matching \mathcal{J}_t (or \mathcal{J}) enforces consistency with the induced evolution of both observables and distributions.

Surrogate generator and objective. Under generator matching, one assumes access to a forward process whose (possibly time-dependent) generator \mathcal{J}_t induces a family of marginals $(p_t)_{t \in [0, 1]}$ that interpolate between p_{init} and p_{data} . Rather than matching vector fields as with flow matching, the objective is to approximate \mathcal{J}_t by a parameterised surrogate generator, \mathcal{J}_t^θ , by minimising a discrepancy between their *generator actions* evaluated at forward samples. For a suitable class of test functionals \mathcal{F} , training takes the form of minimising the loss

$$\mathcal{L}_{\text{GM}}(\theta) = \mathbb{E}_{t \sim \text{Unif}, X_t \sim p_t} [D((\mathcal{J}_t f)(X_t), (\mathcal{J}_t^\theta f)(X_t))], \quad (8)$$

for $f \in \mathcal{F}$ and where $D(\cdot, \cdot)$ denotes a Bregman divergence.

Linear functional parameterisation. In structured-state settings that we consider for G^3 we choose \mathcal{F} to be linear functionals $f_A(X) = \langle A, X \rangle$ (e.g. $\langle A, X \rangle = \text{tr}(A^\top X)$ for matrix states). When there exists an induced operator on states, still denoted \mathcal{J}_t by abuse of notation, such that both

$$\begin{aligned} (\mathcal{J}_t f_A)(X) &= \langle A, \mathcal{J}_t(X) \rangle, \\ (\mathcal{J}_t^\theta f_A)(X) &= \langle A, \mathcal{J}_t^\theta(X) \rangle, \end{aligned}$$

and the objective reduces to the state-space form

$$\mathcal{L}_{\text{GM}}(\theta) = \mathbb{E}_{t \sim \text{Unif}, X_t \sim p_t} \left[D(\mathcal{J}_t(X_t), \mathcal{J}_t^\theta(X_t)) \right], \quad (9)$$

which we will adopt throughout Section 3.

Flow matching can be viewed as a special case of generator matching when the generator corresponds to a deterministic ODE and the divergence is chosen appropriately. However, the generator-centric perspective is more expressive: it captures stochastic dynamics, jump processes, and structured state spaces, and naturally enforces consistency with the Kolmogorov equations governing the underlying process. This makes generator matching particularly appealing to structured data such as graphs, where a meaningful forward process can be directly defined in terms of graph operators. This observation forms the basis of our G^3 method.

3. Graph Generation

We now introduce our generator-based graph generation method G^3 . The construction starts from a graph noising mechanism given by a symmetric Laplacian heat diffusion on matrix-valued graph representations $(Y_s)_{s \in [0, T]}$ (see Section 2.2), and converts this into a $[0, 1]$ -parametrised process $(X_t)_{t \in [0, 1]}$ compatible with generator matching (Section 2.4) via the time-rescaling $X_t := Y_{T(1-t)}$. This yields an explicit ground-truth generator on graph states, which we approximate by a neural surrogate \mathcal{J}_t^θ using a generator matching objective. We then sample new graphs by numerically integrating the learned reverse-time ODE from a simple base distribution.

3.1. Graph Diffusions and Generators

We embed the graph heat diffusion into the generator matching framework of Section 2.4. The key point is that the symmetric heat diffusion admits a closed-form generator; by rescaling time, we obtain a process on $[0, 1]$ consistent with the X -notation used in Sections 2.3–2.4.

Semigroup viewpoint and long-time limit. The forward heat diffusion (2) admits a convenient semigroup interpretation that connects naturally to generator matching and the choice of a simple base state. Define the linear maps, for $s \geq 0$,

$$\mathcal{P}_s(Y) := H_s Y H_s. \quad (10)$$

Then $\{\mathcal{P}_s\}_{s \geq 0}$ is a strongly continuous semigroup on $\mathbb{R}^{n \times n}$, with $\mathcal{P}_0 = \text{Id}$ and $\mathcal{P}_{s+t} = \mathcal{P}_s \circ \mathcal{P}_t$. Moreover, its infinitesimal generator is

$$(\mathcal{G}Y) = -(LY + YL),$$

so that (3) can be written abstractly as $\frac{d}{ds} Y_s = \mathcal{G}Y_s$ (see Lemma A.5 in Appendix A.3).

Limiting behaviour and probabilistic interpretation.

For a connected graph, the Laplacian has a simple eigenvalue at 0 with eigenvector $\mathbf{1}$, and all other eigenvalues are strictly positive; hence

$$\lim_{s \rightarrow \infty} H_s = \Pi := \frac{1}{n} \mathbf{1} \mathbf{1}^\top,$$

the orthogonal projector onto constants. Consequently,

$$\lim_{s \rightarrow \infty} Y_s = \Pi Y_0 \Pi = \frac{1}{n^2} \|Y_0\|_1 \mathbf{1} \mathbf{1}^\top,$$

for non-negative matrices Y_0 . For connected graphs, this convergence is exponentially fast, with rate governed by the spectral gap of the Laplacian (see Lemma A.6 in Appendix A.4). Moreover, when using the random-walk Laplacian L_{rw} , H_s admits the interpretation as the transition kernel of a continuous-time random walk on V (Chung, 1997).

Time rescaling to $[0, 1]$. Generator matching (and flow matching) are formulated on $t \in [0, 1]$ with X_0 drawn from a simple reference distribution and $X_1 \sim p_{\text{data}}$. To align with this convention we define, for a fixed horizon $T > 0$,

$$X_t := Y_{T(1-t)}, \quad t \in [0, 1]. \quad (11)$$

Thus, $X_0 = Y_T$ is a highly diffused (simple) state, while $X_1 = Y_0$ recovers the original graph representation. Differentiating (11) yields

$$\frac{d}{dt} X_t = T(LX_t + X_t L), \quad t \in [0, 1]. \quad (12)$$

Equivalently, in terms of the forward generator \mathcal{G} above, the reverse-time operator satisfies $\mathcal{J} = -T\mathcal{G}$. The forward heat diffusion is contractive; its formal time-reversal corresponds to an anti-diffusive evolution that exponentially amplifies high-frequency (Laplacian eigenmode) components, rendering the exact reverse dynamics ill-posed and numerically unstable (Hadamard, 1923; Evans, 2010) (see Lemma A.7 in Appendix A.4).

Our generator-matching approach circumvents this instability by learning a regularised surrogate generator \mathcal{J}_t^θ from forward-diffused samples, yielding a stable and well-conditioned reverse-time generative sampler.

Infinitesimal generator on states. For linear test functionals $f_A(X) = \langle A, X \rangle := \text{tr}(A^\top X)$ with $A \in \mathbb{R}^{n \times n}$, (12) implies

$$\frac{d}{dt} f_A(X_t) = \left\langle A, \frac{d}{dt} X_t \right\rangle = \langle A, T(LX_t + X_t L) \rangle.$$

Restricting attention to such linear functionals induces a (state-space) time-homogeneous linear operator, which we denote by \mathcal{J} , defined through

$$(\mathcal{J}f_A)(X) = \langle A, \mathcal{J}(X) \rangle = \langle A, T(LX + XL) \rangle. \quad (13)$$

This \mathcal{J} is fully determined by the graph Laplacian and therefore respects permutation equivariance and graph locality by construction.

3.2. Graph Generator Training

Training data and forward diffusion. Let $\{Y_0^{(k)}\}_{k=1}^N$ denote a set of training data graphs, represented as matrices. Define the symmetric heat diffusion

$$Y_s^{(k)} = e^{-sL^{(k)}} Y_0^{(k)} e^{-sL^{(k)}}, \quad s \in [0, T],$$

and the time-rescaled process on $[0, 1]$,

$$X_t^{(k)} := Y_{T(1-t)}^{(k)}, \quad t \in [0, 1].$$

Noised graph training samples are obtained by drawing $t \sim \text{Unif}[0, 1]$ and forming $X_t^{(k)}$ via the above mapping. Throughout, we take the initial graph state to be the adjacency matrix $Y_0^{(k)} = A^{(k)}$ with associated Laplacian $L^{(k)}$. Since all of these objects are symmetric, we retain only the lower-triangular parts of matrices in our implementation, which implicitly removes the presence of any self-loops.

Surrogate generator and objective. From (13), the true generators for training graphs $\{Y_0^{(k)}\}_{k=1}^N$ acting on states are

$$\mathcal{J}^{(k)}(X) = T(L^{(k)}X + XL^{(k)}). \quad (14)$$

Using these target generators, we learn a surrogate generator $\mathcal{J}^\theta : \mathbb{R}^{n \times n} \times [0, 1] \rightarrow \mathbb{R}^{n \times n}$ by minimising

$$\mathbb{E}_k \mathbb{E}_{t \sim \text{Unif}} \left[D(\mathcal{J}^{(k)}(X_t^{(k)}), \mathcal{J}_t^\theta(X_t^{(k)})) \right], \quad (15)$$

where D is a Bregman divergence. In the experiments described in Section 5, we exclusively use mean-squared error loss, $D(A, B) = \|A - B\|_F^2$. See Algorithm 1.

3.3. Sampling via the Reverse-Time ODE

Having learned a surrogate generator \mathcal{J}_t^θ from the forward-noised graphs $\{Y_0^{(k)}, Y_1^{(k)}, \dots, Y_T^{(k)}\}_{k=1}^N$, we generate new graphs under the time-rescaled setting by integrating the

learned ODE from a simple base distribution at $t = 0$ toward a structured graph state at $t = 1$. Note that $t \mapsto X_t = Y_{T(1-t)}$ already reverses the original diffusion time s , so integrating forward in t corresponds to a formal reversal of the heat diffusion in s .

Base distribution. We take p_{init} to be a permutation-symmetric distribution intended to approximate a highly diffused state $X_0 = Y_T$ induced by the forward heat diffusion (cf. Section 2.2). Concretely, we sample an auxiliary matrix $\tilde{X}_0 \in \mathbb{R}^{n \times n}$ by drawing its columns i.i.d. as $\tilde{x}_{0,i} \sim \text{Dirichlet}(\alpha \mathbf{1})$, $i = 1, \dots, n$, enforcing symmetry, and scaling by the average degree $\langle d \rangle := \frac{2}{nN} \sum_{k=1}^N \|Y_0^{(k)}\|_1$:

$$X_0 := \langle d \rangle (\tilde{X}_0 + \tilde{X}_0^\top), \quad (16)$$

with $\alpha > 0$ controlling concentration around the uniform vector. While the exact law of Y_T under the data distribution is intractable, p_{init} provides a simple surrogate capturing permutation symmetry and strong diffusion.

Simulating an ODE on $[0, 1]$. For each training graph k , the time-rescaled heat dynamics satisfy $\frac{d}{dt} X_t^{(k)} = \mathcal{J}^{(k)}(X_t^{(k)})$ with $\mathcal{J}^{(k)}(X) = T(L^{(k)}X + XL^{(k)})$. At generation time we do not condition on a specific Laplacian; instead we integrate the learned surrogate dynamics

$$\frac{d}{dt} X_t = \mathcal{J}_t^\theta(X_t), \quad t \in [0, 1], \quad X_0 \sim p_{\text{init}}, \quad (17)$$

where \mathcal{J}_t^θ has been trained to match the heat-generator action from the forward-diffused states.

Euler discretisation and stabilisation. Fix an integer $M \geq 1$ and set $\delta := 1/M$, with time grid $t_m := m\delta$ for $m = 0, \dots, M$. Approximating X_{t_m} by X^m , explicit Euler integration applied to (17) yields

$$X^{m+1} = X^m + \delta \mathcal{J}_t^\theta(X^m), \quad m = 0, \dots, M-1. \quad (18)$$

To enforce basic validity constraints and improve numerical stability, we optionally apply a projection Π after each step:

$$X^{m+1} = \Pi(X^m + \delta \mathcal{J}_t^\theta(X^m)). \quad (19)$$

Typical projections include symmetrisation $\Pi_{\text{sym}}(Z) = \frac{1}{2}(Z + Z^\top)$, zeroing the diagonal, and element-wise clipping. The final discrete adjacency matrix is obtained by a thresholding operation, $\hat{A}_{ij} = \mathbf{1}\{(\Pi_{\text{sym}} X^M)_{ij} \geq c\}$.

4. Related Work

Beyond the work discussed in Section 1, we highlight several representative graph generation methods. SPECTRE (Martinkus et al., 2022) trains a sequence of GANs to sample eigenvalues and then reconstruct eigenvectors and an

Algorithm 1 G^3 Training

Input: Graph representations $\{Y_0^{(j)}\}_{j=1}^N$, maximum diffusion time T , batch size b , n_{iter} , $\delta > 0$, learning rate η , minimum diffusion time, $\tau := 0.01$

repeat

for batch in batches **do**

 Sample diffusion times: $\{t_i\}_{i=1}^b \sim \text{Unif}[\tau, T]$

 Diffuse states: $\{X_{s_i}^{(i)}\}_{i=1}^b$ for $s_i := 1 - t_i/T$

 Generator targets: $\{T(L_i X_{s_i}^{(i)} + X_{s_i}^{(i)} L_i)\}_{i=1}^b$

 Predict generators: $\{\mathcal{J}_{t_i}^\theta(X_{s_i}^{(i)})\}_{i=1}^b$

 loss = $\frac{1}{b} \sum_{i=1}^b \left\| \mathcal{J}_{t_i}^\theta(X_{s_i}^{(i)}) - \mathcal{J}_{t_i}(X_{s_i}^{(i)}) \right\|_F^2$

if loss unchanged after 10 iterations **then**

$\eta \leftarrow \max\{\eta \times 0.99, 10^{-9}\}$

end if

end for

until loss $< \delta$ or n_{iter} reached

adjacency matrix; the innovation is that spectra encode the salient global topology.

Recent progress has also focused on discrete adaptations of diffusion and flow-matching ideas, including DiGress (Vignac et al., 2022) and DeFoG (Qin et al., 2024). DeFoG achieves strong empirical performance with theoretical guarantees but requires substantial compute, especially on larger graphs, due to its transformer architecture and relative random walk probability features (RRWP).

We use SPECTRE and DeFoG as high-quality, general-purpose baselines. To keep the study computationally tractable, we restrict attention to a small set of competitors and report results from our own reruns of their code, rather than quoting results from earlier papers, to support fair comparisons and reproducibility.

Recent work by (Law et al., 2025) explores the use of heat kernels for graph generation in a related but fundamentally different setting. Their approach targets *directed* graphs and relies on a stochastic heat kernel acting on learned node representations, coupled with a separate edge model that maps these representations back to a valid graph. In contrast, our framework defines and explicitly reverses a diffusion process directly on graph-derived matrix states via generator matching, without introducing an auxiliary edge reconstruction mechanism. As a result, our method applies equally to undirected graphs and, in principle, can be extended to directed settings within the same generator-centric formulation. Moreover, the edge perturbation and reconstruction steps employed in (Law et al., 2025) may alter or obscure global structural constraints, such as planarity, which our Laplacian-based diffusion preserves by construction.

Algorithm 2 G^3 Sampling

Input: Number of new graphs N^* , maximum diffusion time T , number of Euler steps M , base distribution concentration $\alpha > 0$

$\delta \leftarrow 1/M$

$c \leftarrow \frac{1}{n^2 N} \sum_{j=1}^N \|A^{(j)}\|_1$ {Sparsity threshold using average degree}

for $i=0$ to N^* **do**

 Sample $X_0^{(i)} \sim p_{\text{init}}^\alpha$

for $k=0$ to M **do**

$X_{k+1}^{(i)} \leftarrow \Pi_{\text{clip}}(X_k^{(i)} + \delta \mathcal{J}_t^\theta(X_k^{(i)}))$ {Euler steps with element clipping}

end for

$\hat{A}_{ab}^{(i)} \leftarrow \mathbf{1}\{\Pi_{\text{sym}}(X_M^{(i)})_{ab} \geq c\}$ {Symmetrisation; diagonal zeroing; thresholding}

end for

5. Experiments

5.1. Datasets

To assess G^3 performance, we consider three synthetic (SBM, DCSBM, Planar) and three real-world graph datasets (Enzymes, Proteins, QM9), many of which are commonly used for benchmarking in the graph generation literature. The exception is the degree-corrected stochastic block model (DCSBM) dataset, which allows for more reasonable models of community-structured networks (Karrer & Newman, 2011). Details are provided in Section B.

5.2. Evaluation

To evaluate G^3 graph generation performance, we rely on the maximum mean discrepancy (MMD) of various graph attributes between hold-out samples of graphs and our generated samples, as is standard in the literature. Effectiveness is assessed by comparing the attribute distribution between hold-out test graphs and generated graphs for the following five graph characteristics: clustering coefficient, degree distribution, 4-node orbit count, graph Laplacian spectrum and triangle counts. Further details are provided in Section C.

5.3. Neural Network Architecture

The G^3 generator surrogate \mathcal{J}_t^θ trained using Algorithm 1 is a simple 4-layer MLP neural network with ReLU activation functions and layer normalisation. The network acts on the flattened form of the diffused network input state that is reshaped into a square matrix for output. In general, there are 4096 units per hidden layer, where the sensitivity of this design choice is explored in Section 5.4. Further details are provided in Section D.

5.4. Graph Generation Sensitivity

To understand how sensitive G^3 is to graph topology, training dynamics and hyperparameters, we consider how effective the methodology is as these factors are systematically varied. We focus on the spectral MMD as the most comprehensive single metric over which to assess sensitivity. Additional figures are provided in Section F.

Sensitivity to maximum diffusion time. Figure 2 shows an example of how spectral MMD is sensitive to the choice of T , the maximum time states are diffused to during the forward training process and its dependence on the number of graphs, N . This provides us with a simple general principle that T should increase with training set size, avoiding the need to treat this as a tunable hyperparameter.

Figure 5a demonstrates less dependence on the number of nodes, n , than might have been expected; we can broadly opt to neglect its influence on this same choice of parameter. The minimum of the curves seems to occur at approximately the same T , indicating that the number of graphs, N , is the more important factor and that the problem gets “harder” as n increases, at least for planar graphs.

Sensitivity to neural network architecture. Figure 3 shows an example of how spectral MMD is sensitive to the choice of the number of hidden neural network units per layer of the MLP, w , and its dependence on the number of graphs, N . The minimum occurs at approximately $2^{12} = 4096$ hidden units, independent of N .

Based on this independence, Figure 6a computes a small table for SBMs with fixed N for use across all other datasets in our further experiments to save unnecessary computation. In other words, we do not tune the neural network architecture for each dataset in turn.

Sensitivity to base distribution. Figure 9 shows how the choice of hyperparameter α in the base sampling distribution affects the efficacy of the model for SBM and planar graphs. The choice of α not only affects the spectral performance but also the ability to generate unique new graphs (see Figure 10).

Empirically, $\alpha < 1$ is preferable for planar-like graphs including the biomolecular datasets, while for community-like graphs such as SBM and DCSBM, $\alpha = 1$ is preferable.

5.5. Performance

We now compare the performance of G^3 , using both symmetric and asymmetric formulations of the heat diffusion strategy, to both SPECTRE and DeFoG over a selection of synthetic and real-world datasets. The asymmetric version

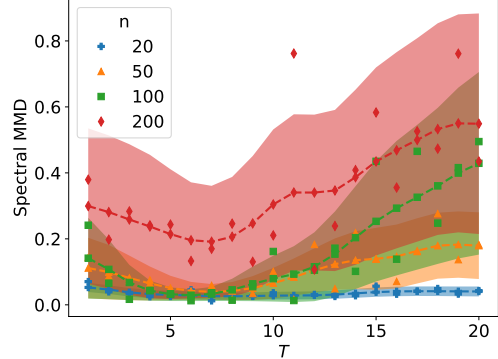


Figure 2. Spectral MMD as a function of maximum diffusion time T and the number of planar graphs N with $n = 64$ nodes. Curves are Gaussian-smoothed¹ functions of the observations shown, which themselves are averaged over 10 random seeds. Shaded regions indicate 66% confidence intervals under CLT assumptions. Learning rate set at 1×10^{-4} for training.

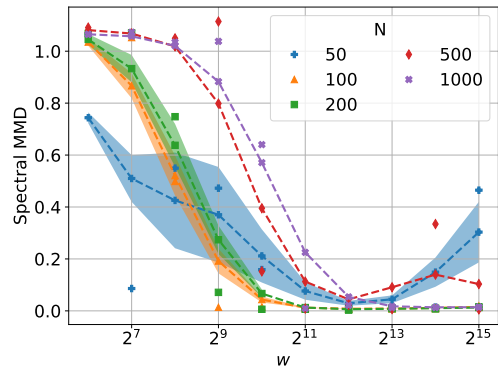


Figure 3. Spectral MMD as a function of the number of hidden neural network units per layer w and the number of planar graphs N with $n = 64$ nodes. Curves are Gaussian-smoothed¹ functions of the observations shown, which themselves are averaged over 10 random seeds. Shaded regions indicate 66% confidence intervals under CLT assumptions. Learning rate set at 1×10^{-4} for training.

of G^3 is outlined in Section E.1.

We compute the median \pm median absolute deviation of the MMD between hold-out test graphs and generated graphs reported in Table 1, where lower quantities are better. Although there is no clear winner over all of the datasets and metrics, G^3 is not only competitive, but *substantially* faster to run. Training and generation time per sample graph takes seconds for G^3 compared to 15-30 minutes for DeFoG and SPECTRE (see Figure 11).

To highlight this point, we repeated the DeFoG and SPECTRE experiments on datasets where they previously performed well, but under reduced computational budgets. The number of training epochs was decreased by a factor of 10-100, although their total training times still generally exceeded those of G^3 . We denote these constrained variants by DeFoG* and SPECTRE* and report the results in

¹Using `gaussian_filter1d` function from SciPy package.

Table 1. Median (\pm median abs. deviation) of MMD metrics for G^3 , DeFoG, SPECTRE over 3 – 5 randomly seeded splits. Lower is better and **bold** indicates best performance; *italics* second-best performance, based on the median plus one median abs. deviation.

Dataset	Model	Clustering	Degree	Orbit	Spectrum	Triangles
SBM	G^3	0.0356 ± 0.0005	0.0318 ± 0.0052	0.0631 ± 0.0120	0.0796 ± 0.0120	0.0270 ± 0.0078
	Asymm. G^3	0.0398 ± 0.0010	0.0390 ± 0.0052	0.0710 ± 0.0140	0.0832 ± 0.0015	0.0287 ± 0.0084
	DeFoG	0.0500 ± 0.0000	0.0258 ± 0.0190	0.0500 ± 0.0000	0.0884 ± 0.0740	0.0097 ± 0.0083
	SPECTRE	0.0588 ± 0.0089	0.2030 ± 0.1700	0.0500 ± 0.0000	0.7010 ± 0.4800	0.3320 ± 0.2300
DCSBM	G^3	0.1270 ± 0.0091	0.0344 ± 0.0062	0.0971 ± 0.0057	0.1230 ± 0.0330	0.0110 ± 0.0098
	Asymm. G^3	0.2340 ± 0.0160	0.0810 ± 0.0200	0.1420 ± 0.0170	0.1010 ± 0.0220	0.0578 ± 0.0250
	DeFoG	0.0556 ± 0.0067	0.0063 ± 0.0050	0.0591 ± 0.0110	0.0499 ± 0.0240	0.0006 ± 0.0002
	SPECTRE	1.0800 ± 0.0340	0.6640 ± 0.0007	1.0400 ± 0.0004	1.2500 ± 0.0250	0.7340 ± 0.0130
Planar	G^3	0.3090 ± 0.0300	0.0030 ± 0.0015	0.0035 ± 0.0018	0.0060 ± 0.0015	0.0467 ± 0.0360
	Asymm. G^3	1.0200 ± 0.0440	0.0074 ± 0.0050	0.0106 ± 0.0089	0.0113 ± 0.0021	0.1110 ± 0.0320
	DeFoG	0.0413 ± 0.0047	0.0007 ± 0.0001	0.0002 ± 0.0000	0.0006 ± 0.0003	0.0056 ± 0.0013
	SPECTRE	0.1420 ± 0.0220	0.0242 ± 0.0190	0.4240 ± 0.3800	0.0560 ± 0.0019	0.0226 ± 0.0026
Enzymes	G^3	0.0225 ± 0.0008	0.0854 ± 0.0550	0.0902 ± 0.0390	0.0755 ± 0.0220	0.0490 ± 0.0380
	Asymm. G^3	0.0803 ± 0.0200	0.0934 ± 0.0520	0.1040 ± 0.0047	0.1090 ± 0.0480	0.0752 ± 0.0120
	DeFoG	0.0765 ± 0.0036	0.7220 ± 0.0070	0.5530 ± 0.0140	1.2000 ± 0.0270	0.4650 ± 0.0033
	SPECTRE	0.0275 ± 0.0002	0.0168 ± 0.0013	0.0796 ± 0.0120	0.0490 ± 0.0030	0.0236 ± 0.0029
Proteins	G^3	0.0465 ± 0.0009	0.0220 ± 0.0012	0.5530 ± 0.0720	0.1600 ± 0.0074	0.0928 ± 0.018
	Asymm. G^3	0.0750 ± 0.0073	0.0345 ± 0.0003	0.3480 ± 0.2000	0.0921 ± 0.0110	0.0419 ± 0.0071
	DeFoG	0.1050 ± 0.0032	0.7500 ± 0.0003	1.2700 ± 0.0000	1.2000 ± 0.0110	0.5800 ± 0.0006
	SPECTRE	0.1070 ± 0.0001	0.0867 ± 0.0480	0.8400 ± 0.0085	0.1310 ± 0.0430	0.1240 ± 0.0110
QM9	G^3	0.2530 ± 0.0074	0.1870 ± 0.0400	0.1650 ± 0.0330	0.1100 ± 0.0027	0.1100 ± 0.0066
	Asymm. G^3	0.0834 ± 0.0170	0.0214 ± 0.0033	0.0036 ± 0.0013	0.0168 ± 0.0033	0.0521 ± 0.0130
	DeFoG	0.5460 ± 0.3000	0.0449 ± 0.0170	0.0036 ± 0.0001	0.0640 ± 0.0049	0.1730 ± 0.0950
	SPECTRE	0.0200 ± 0.0110	0.0027 ± 0.0001	0.0008 ± 0.0001	0.0046 ± 0.0003	0.0051 ± 0.0043

Table 7. Under these conditions, G^3 tends to outperform the alternative methods, particularly with respect to degree distribution and spectral accuracy.

Although on the whole the symmetric heat diffusion leads to better performance than the asymmetric version, there is no great margin, and on certain datasets (QM9, Enzymes and Proteins) the asymmetric process is preferred. One might suppose that biomolecular structures lend themselves more to the asymmetric approach, although the superior performance of the symmetric version on the planar synthetic dataset effectively rules out planarity as an explanation.

6. Discussion

In this work, we have introduced a novel, well-grounded framework for graph generation by integrating symmetric heat diffusion with generator matching. The use of the graph Laplacian as the generator injects domain-specific inductive bias, ensuring that the noising process inherently respects graph topology (e.g., local connectivity and geometry). Empirically, we have shown, via controlled simulation studies and real-world graph generation benchmarks, that our method is competitive and highly scalable.

An appealing aspect of this methodology is the number of

avenues for further development. Our general framework is permutation-invariant in construction, but our current implementation uses a simple MLP for generator matching. While the experiments show success in this simple setting, we believe this could be further improved by using a permutation-equivariant neural network architecture such as GNNs.

The theoretical framework outlined in Section 3.2–3.3 relies on the heat kernel associated with the combinatorial graph Laplacian. Alternatives such as the random walk Laplacian could be used, as the underlying G^3 framework is more general (as motivated in Section E.2).

Relatedly, we focus on a symmetric form of heat diffusion on undirected graphs, but by relaxing the symmetry assumption we could extend this work to directed graphs. In a similar vein, we expect other more exotic structures, including hypergraphs, to be amenable to the G^3 strategy too via a suitable hypergraph Laplacian.

An extension of particular interest to the authors is to incorporate graph and node covariate information for conditional generation, known as “guidance” in the generative literature. A toy example of how this might work is provided in Section E.3, where we generate sample SBMs with pre-specified group membership.

Acknowledgements

CN gratefully acknowledges the support of EPSRC grants EP/V022636/1 and EP/Y028783/1. This work was also supported by Research England under the Expanding Excellence in England (E3) funding stream, which was awarded to MARS: Mathematics for AI in Real-world Systems in the School of Mathematical Sciences at Lancaster University.

Impact Statement

This paper presents a broad and adaptable framework for generating graphs, aiming to support a wide range of applications that include drug discovery, general graph synthesis, circuit design and cybersecurity. Advances in graph generation hold the potential to influence many scientific and technological fields and may carry both beneficial and challenging societal or ethical implications, particularly within biomedical and chemical research. However, at this stage, we do not anticipate any immediate societal concerns related to the methods introduced here.

References

Binkiewicz, N., Vogelstein, J. T., and Rohe, K. Covariate-assisted spectral clustering. *Biometrika*, 104(2):361–377, 2017.

Brown, N., Fiscato, M., Segler, M. H., and Vaucher, A. C. GuacaMol: Benchmarking models for de novo molecular design. *Journal of chemical information and modeling*, 59(3):1096–1108, 2019.

Chen, R. T. Q., Rubanova, Y., Bettencourt, J., and Duvenaud, D. Neural ordinary differential equations. *arXiv preprint arXiv:1806.07366*, 2018.

Chung, F. R. *Spectral graph theory*, volume 92. American Mathematical Soc., 1997.

De Cao, N. and Kipf, T. MolGAN: An implicit generative model for small molecular graphs. *arXiv preprint arXiv:1805.11973*, 2018.

Evans, L. C. *Partial Differential Equations*. American Mathematical Society, 2 edition, 2010.

Forman. Bochner’s method for cell complexes and combinatorial Ricci curvature. *Discrete & Computational Geometry*, 29(3):323–374, 2003.

Fu, D., Bao, W., Maciejewski, R., Tong, H., and He, J. Privacy-preserving graph machine learning from data to computation: A survey. *ACM SIGKDD Explorations Newsletter*, 25(1):54–72, 2023.

Hadamard, J. *Lectures on Cauchy’s Problem in Linear Partial Differential Equations*. Yale University Press, 1923.

Holderrieth, P., Havasi, M., Yim, J., Shaul, N., Gat, I., Jaakkola, T., Karrer, B., Chen, R. T., and Lipman, Y. Generator matching: Generative modeling with arbitrary markov processes. *arXiv preprint arXiv:2410.20587*, 2024.

Ji, S., Pan, S., Cambria, E., Marttinen, P., and Yu, P. S. A survey on knowledge graphs: Representation, acquisition, and applications. *IEEE transactions on neural networks and learning systems*, 33(2):494–514, 2021.

Jo, J., Lee, S., and Hwang, S. J. Score-based generative modeling of graphs via the system of stochastic differential equations. In *International conference on machine learning*, pp. 10362–10383. PMLR, 2022.

Karrer, B. and Newman, M. E. Stochastic blockmodels and community structure in networks. *Physical Review E—Statistical, Nonlinear, and Soft Matter Physics*, 83(1):016107, 2011.

Kipf, T. N. and Welling, M. Variational graph auto-encoders. *arXiv preprint arXiv:1611.07308*, 2016.

Law, M. T., Kreis, K., and Maron, H. Directed graph generation with heat kernels. *Transactions on Machine Learning Research*, 2025.

Lipman, Y., Chen, R. T., Ben-Hamu, H., Nickel, M., and Le, M. Flow matching for generative modeling. *arXiv preprint arXiv:2210.02747*, 2022.

Martinkus, K., Loukas, A., Perraudin, N., and Wattenhofer, R. SPECTRE: Spectral conditioning helps to overcome the expressivity limits of one-shot graph generators. In *International Conference on Machine Learning*, pp. 15159–15179. PMLR, 2022.

Morris, C., Kriege, N. M., Bause, F., Kersting, K., Mutzel, P., and Neumann, M. TUDataset: A collection of benchmark datasets for learning with graphs. *arXiv preprint arXiv:2007.08663*, 2020.

Nettleton, D. F. Data mining of social networks represented as graphs. *Computer Science Review*, 7:1–34, 2013.

Qin, Y., Madeira, M., Thanou, D., and Frossard, P. De-FoG: Discrete flow matching for graph generation. *arXiv preprint arXiv:2410.04263*, 2024.

Schneider, E. W. Course modularization applied: The interface system and its implications for sequence control and data analysis. 1973.

Song, Y., Sohl-Dickstein, J., Kingma, D. P., Kumar, A., Ermon, S., and Poole, B. Score-based generative modeling through stochastic differential equations. *arXiv preprint arXiv:2011.13456*, 2020.

Sriperumbudur, B. K., Gretton, A., Fukumizu, K., Schölkopf, B., and Lanckriet, G. R. Hilbert space embeddings and metrics on probability measures. *The Journal of Machine Learning Research*, 11:1517–1561, 2010.

Sylvester, J. Chemistry and algebra. *Nature*, 17:284–284, 1878.

Thompson, R., Knyazev, B., Ghalebi, E., Kim, J., and Taylor, G. W. On evaluation metrics for graph generative models. *arXiv preprint arXiv:2201.09871*, 2022.

Tolstikhin, I. O., Sriperumbudur, B. K., and Schölkopf, B. Minimax estimation of maximum mean discrepancy with radial kernels. *Advances in Neural Information Processing Systems*, 29, 2016.

Vignac, C., Krawczuk, I., Siraudin, A., Wang, B., Cevher, V., and Frossard, P. DiGress: Discrete denoising diffusion for graph generation. *arXiv preprint arXiv:2209.14734*, 2022.

Wang, H., Wang, J., Wang, J., Zhao, M., Zhang, W., Zhang, F., Xie, X., and Guo, M. GraphGAN: Graph representation learning with generative adversarial nets. In *Proceedings of the AAAI conference on artificial intelligence*, volume 32, 2018.

Wills, P. and Meyer, F. G. Metrics for graph comparison: a practitioner’s guide. *Plos one*, 15(2):e0228728, 2020.

Wu, Z., Ramsundar, B., Feinberg, E. N., Gomes, J., Geniesse, C., Pappu, A. S., Leswing, K., and Pande, V. MoleculeNet: A benchmark for molecular machine learning. *Chemical science*, 9(2):513–530, 2018.

Yang, L., Zhang, Z., Zhang, W., and Hong, S. Score-based graph generative modeling with self-guided latent diffusion. 2023.

You, J., Ying, R., Ren, X., Hamilton, W., and Leskovec, J. GraphRNN: Generating realistic graphs with deep auto-regressive models. In *International conference on machine learning*, pp. 5708–5717. PMLR, 2018.

Zheng, X., Zhang, M., Chen, C., Molaei, S., Zhou, C., and Pan, S. GNNEvaluator: Evaluating GNN performance on unseen graphs without labels. *Advances in Neural Information Processing Systems*, 36:33606–33623, 2023.

A. Proofs and Further Details

A.1. Heat Equation and Heat Kernel

Proposition A.1 (Solution of the symmetric heat diffusion via the heat kernel). *Let $L \in \mathbb{R}^{n \times n}$ be the (combinatorial) Laplacian of an undirected graph, and define the heat kernel $H_s := e^{-sL}$ for $s \geq 0$. For any initial matrix $Y_0 \in \mathbb{R}^{n \times n}$, the matrix-valued symmetric heat equation*

$$\frac{d}{ds} Y_s = -(LY_s + Y_s L), \quad s \geq 0, \quad (20)$$

admits the unique solution

$$Y_s = H_s Y_0 H_s = e^{-sL} Y_0 e^{-sL}, \quad s \geq 0. \quad (21)$$

In particular, the family of linear maps $(\mathcal{P}_s)_{s \geq 0}$ defined by $\mathcal{P}_s(Y) := H_s Y H_s$ forms the (matrix) heat semigroup associated with the generator $Y \mapsto LY + YL$.

Proof. Since L is real symmetric, it is orthogonally diagonalizable: $L = U\Lambda U^\top$ with U orthonormal and $\Lambda = \text{diag}(\lambda_1, \dots, \lambda_n)$, $\lambda_i \geq 0$. Hence

$$H_s := e^{-sL} = U e^{-s\Lambda} U^\top, \quad \text{and} \quad \frac{d}{ds} H_s = -LH_s = -H_s L.$$

Define $Y_s := H_s Y_0 H_s$. Differentiating and using the product rule,

$$\frac{d}{ds} Y_s = \left(\frac{d}{ds} H_s \right) Y_0 H_s + H_s Y_0 \left(\frac{d}{ds} H_s \right) = (-LH_s) Y_0 H_s + H_s Y_0 (-H_s L) = -(LY_s + Y_s L),$$

so Y_s satisfies (3). Moreover $Y_0 = H_0 Y_0 H_0 = Y_0$. Uniqueness follows from standard linear ODE theory on $\mathbb{R}^{n \times n}$ (equivalently, by vectorizing the equation to a linear system on \mathbb{R}^{n^2}). \square

A.2. Dissipativity and Stability of the Symmetric Heat Diffusion

In Section 2.2 we consider the matrix-valued heat equation

$$\frac{d}{ds} Y_s = -(LY_s + Y_s L), \quad Y_0 \in \mathbb{R}^{n \times n}, \quad (22)$$

where $L \in \mathbb{R}^{n \times n}$ is the (combinatorial) graph Laplacian of an undirected graph, hence symmetric positive semidefinite.

We equip $\mathbb{R}^{n \times n}$ with the Frobenius inner product

$$\langle A, B \rangle_F := \text{tr}(A^\top B), \quad \|A\|_F^2 := \langle A, A \rangle_F.$$

Define the linear operator $\mathcal{A} : \mathbb{R}^{n \times n} \rightarrow \mathbb{R}^{n \times n}$ by

$$\mathcal{A}(Y) := LY + YL, \quad \text{and} \quad \mathcal{G}(Y) := -\mathcal{A}(Y) = -(LY + YL).$$

Lemma A.2 (Dissipativity of the symmetric heat operator). *If L is symmetric positive semidefinite, then \mathcal{G} is dissipative with respect to $\langle \cdot, \cdot \rangle_F$, i.e.*

$$\langle \mathcal{G}(Y), Y \rangle_F \leq 0 \quad \text{for all } Y \in \mathbb{R}^{n \times n}.$$

Equivalently, $\langle \mathcal{A}(Y), Y \rangle_F \geq 0$ for all Y .

Proof. We compute

$$\langle \mathcal{A}(Y), Y \rangle_F = \langle LY, Y \rangle_F + \langle YL, Y \rangle_F = \text{tr}(Y^\top LY) + \text{tr}(Y^\top YL).$$

For the first term, write $Y = [y_1, \dots, y_n]$ in columns. Then

$$\text{tr}(Y^\top LY) = \sum_{j=1}^n y_j^\top Ly_j \geq 0$$

since $L \succeq 0$ (i.e. positive semidefinite).

For the second term, note that $Y^\top Y \succeq 0$ and $L \succeq 0$. Using the identity

$$\text{tr}(AB) = \|A^{1/2}B^{1/2}\|_F^2 \quad \text{for } A \succeq 0, B \succeq 0,$$

we obtain

$$\text{tr}(Y^\top Y L) = \text{tr}((Y^\top Y)L) \geq 0.$$

Hence $\langle \mathcal{A}(Y), Y \rangle_F \geq 0$ and therefore $\langle \mathcal{G}(Y), Y \rangle_F = -\langle \mathcal{A}(Y), Y \rangle_F \leq 0$. \square

Corollary A.3 (Energy dissipation and Frobenius stability). *Let $(Y_s)_{s \geq 0}$ solve (22). Then the Frobenius norm is nonincreasing:*

$$\frac{d}{ds} \|Y_s\|_F^2 = 2\langle \dot{Y}_s, Y_s \rangle_F = 2\langle \mathcal{G}(Y_s), Y_s \rangle_F \leq 0, \quad \text{hence} \quad \|Y_s\|_F \leq \|Y_0\|_F \quad \forall s \geq 0.$$

In particular, (22) defines a stable linear diffusion on $\mathbb{R}^{n \times n}$ in the sense of contraction in $\|\cdot\|_F$.

Proof. Differentiate $\|Y_s\|_F^2$ and apply Lemma A.2. \square

Lemma A.4 (Closed-form solution and semigroup contraction). *Let $H_s := e^{-sL}$. The unique solution to (22) is*

$$Y_s = H_s Y_0 H_s, \quad s \geq 0.$$

Moreover, the maps $\mathcal{P}_s(Y) := H_s Y H_s$ form a strongly continuous semigroup on $\mathbb{R}^{n \times n}$ and satisfy the contraction bound

$$\|\mathcal{P}_s(Y)\|_F \leq \|Y\|_F, \quad s \geq 0.$$

Proof. The representation $Y_s = H_s Y_0 H_s$ follows by differentiating $H_s Y_0 H_s$ and using $\frac{d}{ds} H_s = -LH_s = -H_s L$. For contraction, since L is symmetric with eigenvalues $\lambda_i \geq 0$, the eigenvalues of H_s are $e^{-s\lambda_i} \in (0, 1]$, hence $\|H_s\|_2 \leq 1$.

Recall the submultiplicativity result for the Frobenius norm. For all matrices A and B , $\|AB\|_F^2 = \text{tr}(B^\top A^\top AB)$. Now since $\|A\|_2^2 I \succeq A^\top A$, we obtain $\text{tr}(B^\top A^\top AB) \leq \|A\|_2^2 \text{tr}(B^\top B) = \|A\|_2^2 \|B\|_F^2$. Taking square roots yields the result $\|AB\|_F \leq \|A\|_2 \|B\|_F$. Using this result, we therefore have,

$$\|H_s Y H_s\|_F \leq \|H_s\|_2 \|Y H_s\|_F \leq \|H_s\|_2^2 \|Y\|_F \leq \|Y\|_F. \quad \square$$

A.3. Semigroups and Infinitesimal Generators

Lemma A.5 (Semigroup structure and infinitesimal generator). *Let $\{H_s\}_{s \geq 0}$ be the graph heat kernel $H_s = e^{-sL}$ and define the family of linear operators*

$$P_s : \mathbb{R}^{n \times n} \rightarrow \mathbb{R}^{n \times n}, \quad P_s(Y) := H_s Y H_s.$$

Then $\{P_s\}_{s \geq 0}$ forms a strongly continuous one-parameter semigroup on $\mathbb{R}^{n \times n}$ with $P_0 = \text{Id}$ and $P_{s+t} = P_s \circ P_t$. Its infinitesimal generator \mathcal{A} is the linear operator

$$\mathcal{A}(Y) = LY + YL,$$

with domain $\text{Dom}(\mathcal{A}) = \mathbb{R}^{n \times n}$, and the symmetric heat equation

$$\frac{d}{ds} Y_s = -\mathcal{A}(Y_s)$$

is the abstract evolution equation associated with this semigroup.

Proof. The semigroup property follows directly from $H_{s+t} = H_s H_t$:

$$P_{s+t}(Y) = H_{s+t} Y H_{s+t} = H_s (H_t Y H_t) H_s = (P_s \circ P_t)(Y),$$

and $P_0(Y) = IYI = Y$. Strong continuity holds since $s \mapsto H_s$ is continuous in operator norm.

For the generator, compute for any $Y \in \mathbb{R}^{n \times n}$,

$$\lim_{h \downarrow 0} \frac{P_h(Y) - Y}{h} = \lim_{h \downarrow 0} \frac{H_h Y H_h - Y}{h} = -LY - YL,$$

using $H_h = I - hL + o(h)$. Thus $\mathcal{A}(Y) = LY + YL$. \square

A.4. Results for the Forward and Reverse Processes

Lemma A.6. *For a connected graph with combinatorial Laplacian L , the Frobenius norm between the symmetric heat diffusion $Y_T = H_T Y_0 H_T$ and its forward process limit $\lim_{s \rightarrow \infty} Y_s = \Pi Y_0 \Pi$ satisfies*

$$\|Y_T - \Pi Y_0 \Pi\|_F \leq 2e^{-T\lambda_2} \|Y_0\|_F,$$

where λ_2 is the smallest non-zero eigenvalue of L .

Proof. Consider the decomposition

$$\begin{aligned} \|Y_T - \Pi Y_0 \Pi\|_F &= \|H_T Y_0 H_T - \Pi Y_0 \Pi\|_F \\ &\leq \|H_T Y_0 H_T - \Pi Y_0 H_T\|_F + \|\Pi Y_0 H_T - \Pi Y_0 \Pi\|_F \\ &= \|(H_T - \Pi) Y_0 H_T\|_F + \|\Pi Y_0 (H_T - \Pi)\|_F \\ &\leq \|H_T - \Pi\|_2 \|Y_0\|_F \|H_T\|_2 + \|\Pi\|_2 \|Y_0\|_F \|H_T - \Pi\|_2, \end{aligned}$$

using the property that, for arbitrary matrices, $\|ABC\|_F \leq \|A\|_2 \|B\|_F \|C\|_2$.

Π is the rank-1 projection onto constants $\frac{1}{n}\mathbf{1}\mathbf{1}^\top$ with eigenvalue 1, which implies that $\|\Pi\|_2 = 1$. $H_T = e^{-TL}$ has eigenvalues $e^{-T\lambda_i}$ which implies that $\|H_T\|_2 = 1$. Since $\mathbf{1}$ is an eigenvector of both e^{-TL} and Π with eigenvalue 1, $H_T - \Pi$ can be simultaneously diagonalised. Therefore $\|H_T - \Pi\|_2 = e^{-T\lambda_2}$ corresponding to the smallest non-zero eigenvalue of L . Substituting these equalities into the starting decomposition completes the proof. \square

Lemma A.7. *Let $X_0 = \Pi + X_\perp$ be an initial state for the reverse-time ODE where X_\perp has row sums and column sums equal to 0, namely $\mathbf{1}^\top X_\perp = \mathbf{0}$ and $X_\perp \mathbf{1} = \mathbf{0}$. Reversing the heat diffusion with the true generator $\mathcal{J}X = T(LX + XL)$ produces $X_1 = e^{TL} X_0 e^{TL}$ satisfying*

$$\|X_1\|_F \geq e^{2T\lambda_2} \|X_\perp\|_F.$$

Proof. Observe that

$$X_1 = e^{TL}(\Pi + X_\perp)e^{TL} = \Pi + e^{TL}X_\perp e^{TL},$$

since $\mathbf{1}$ is an eigenvector of e^{TL} with eigenvalue 1. Therefore, $\|X_1\|_F \geq \|e^{TL}X_\perp e^{TL}\|_F$.

Let $L = U\Lambda U^\top$ be the eigendecomposition of L , meaning $e^{TL} = Ue^{T\Lambda}U^\top$. Therefore,

$$\|e^{TL}X_\perp e^{TL}\|_F^2 = \|e^{T\Lambda}U^\top X_\perp U e^{T\Lambda}\|_F^2 = \sum_{i,j} e^{2T(\lambda_i + \lambda_j)} (U^\top X_\perp U)_{ij}.$$

Since $\mathbf{1}$ is the eigenvalue of L corresponding to $\lambda_1 = 0$, this implies that both $(U^\top X_\perp U)_{ij} = 0$ and $(U^\top X_\perp U)_{1j} = 0$ meaning the λ_1 terms do not contribute to the sum. For the remaining non-zero terms $\lambda_i + \lambda_j \geq 2\lambda_2$, therefore

$$\|e^{TL}X_\perp e^{TL}\|_F^2 \geq e^{4T\lambda_2} \sum_{i,j} (U^\top X_\perp U)_{ij} = e^{4T\lambda_2} \|X_\perp\|_F^2.$$

Taking square roots completes the proof. \square

B. Datasets

For all datasets listed below, when running experiments as described in Section 5.4, or for choosing hyperparameters, we use random seeds in the range 10 – 20. For model benchmarking we use seeds 1 – 5.

B.1. Synthetic

SBM We generate random stochastic block model networks (SBMs) with consistent intra-community and inter-community edge probabilities given by $p_{\text{inter}} = 0.05$ and $p_{\text{intra}} = 0.3$ to allow for reasonable distinguishability of communities. The number of communities is selected at random from $\{2, 3, 4, 5\}$. For general analysis we construct any number of such graphs with arbitrary numbers of nodes using random seeds to control reproducibility. For benchmarking, we retained the seeds 1 – 5 and split sets of $N = 200$, 200-node graphs into 80% training data and 20% test.

DCSBM Degree-corrected SBMs, where the general construction mirrors that of standard SBMs but with additional control over the degree distribution, are generally considered to be more reasonable models for community-structured networks. Our datasets of such graphs are constructed using the same setup as for the SBMs outlined above but with edge probabilities weighted by draws from a Beta(1, 1) distribution.

Planar Alongside the stochastic block models described above, we also included planar graphs as an important case study in their own right and as a stark topologically different challenge. In this case we constructed planar graphs by sampling uniformly at random 2D points and connecting this via Delaunay triangulation. As above, for general analysis we generated any number of n -node planar graphs, retaining specific datasets of $N = 200$, $n = 64$ with the same random seeds and train/test splits as above.

B.2. Real-world

For the purposes of benchmarking on real-world graph datasets, we make use of the popular TUDataset, introduced in (Morris et al., 2020), via the PyTorch Geometric library due to its convenient interface.

Proteins Macromolecules represent a rich set of variable-size graphs that include as a subset planar networks. Graphs are constructed by connecting edges between molecular substructures if they neighbour one another along a sequence of amino acids or are one of three nearest-neighbours in space. The dataset was originally introduced as an example problem of identifying enzymes from a set of macromolecules.

Enzymes This dataset is much like the proteins dataset, only now all of the elements are enzymes (and the original task was to classify their type).

QM9 Molecular data constitutes a significant example of real-world planar graphs and generating such graphs is a frequent objective in the community. We follow suit and include the QM9 (Wu et al., 2018) dataset, consisting of small organic molecules ($n \leq 9$), along with additional molecular attributes. Following the likes of SPECTRE and DeFoG, we randomly partition the data into training, validation and test sets of size 97,682, 20,026 and 13,123 respectively. At generation time, 512 samples are produced (from each model) to compare to the test set. Test metrics are computed over a maximum of 500 graphs from the test set, to reduce computation time.

C. Evaluation

To evaluate the performance of our generator matching model we use synthetic and real-world graph datasets. Having defined a training set of graphs, we follow the procedure described in Section 3.2 to train a neural generator and subsequently produce new graphs by sampling from a suitable limiting distribution (corresponding to the choice of generator) and reversing the diffusion process.

Our goal is to create new sets of graphs whose properties closely resemble those from the training set. Due to the complex structure of networks, defining what those properties should be is in general non-trivial. Substantial effort has been devoted to defining such properties across various mathematical disciplines that make use of such data structures. Within the statistical and machine learning community, we highlight work such as: (Wills & Meyer, 2020), in which the authors discuss various commonly used metrics and their relationship to topological features; (Thompson et al., 2022), which introduces metrics specifically intended to aid in measuring the performance of graph-generative models; (Zheng et al., 2023) which focuses on evaluating the performance of GNNs at node-classification tasks.

Following the approach of precursory generative graph models, we adopt the use of maximum mean discrepancy (MMD) as a way to numerically evaluate the difference between empirical distributions of characteristics.

The basis of the MMD is in the embedding of probability measures in a reproducing kernel Hilbert space (RKHS). More precisely, given a probability measure P , continuous positive-definite real-valued kernel k defined on a (separable) topological space \mathcal{X} with corresponding RKHS \mathcal{H} , the kernel mean embedding of P is given by $\mu_P := \int k(\cdot, x)dP(x)$, provided k is P -integrable. With this in mind, we define the MMD between measures P and Q as

$$\text{MMD}(P, Q) := \|\mu_P - \mu_Q\|_{\mathcal{H}}.$$

In practice, we usually approximate μ_P by the Monte Carlo estimate $\mu_{P_n} = \frac{1}{n} \sum_{i=1}^n k(\cdot, X_i)$ with the use of the kernel trick:

$$\text{MMD}^2(P, Q) = \mathbb{E}_{X, X'} \{k(X, X')\} + \mathbb{E}_{Y, Y'} \{k(Y, Y')\} - 2 \mathbb{E}_{X, Y} \{k(X, Y)\}$$

where expectations are approximated with Monte Carlo estimates with $X, X' \sim P$ and $Y, Y' \sim Q$. In our case, each contribution to the Monte Carlo estimate corresponds to evaluating the kernel over pairwise empirical distributions of graph properties listed below, each computed from singular graphs.

We leave detailed analysis of this metric (and its estimators) to the likes of (Sriperumbudur et al., 2010) and (Tolstikhin et al., 2016) but suffice to note that generally one should choose a *universal* kernel so that \mathcal{H} is *characteristic* in the sense that $\text{MMD}(P, Q) = 0 \iff P = Q$; i.e. $\text{MMD}(\cdot, \cdot)$ is a valid metric.

We use MMD to measure the similarity between generated sets of graphs and hold-out graphs (from the relevant dataset) on the following characteristics:

Degree: For a node i , the degree, d_i , denotes the number of edges connected to it.

Triangles: T_i represents the number of triangles for which i is a vertex.

Clustering (coefficient): The clustering coefficient for node i is given by $c_i = 2T_i/d_i(d_i - 1)$.

Orbit: Specifically 4-node orbit counts: the number of occurrences of each orbit for graphlets of (upto) size 4.

Spectrum: The eigenvalues, λ_i , of the (normalised) graph Laplacian define the spectrum for the purposes of MMD evaluation.

D. Implementation Details

D.1. Neural Network Architecture

Our neural generator is a simple 4-layer ReLU MLP with (in general) 4096 nodes per hidden layer and layer normalisation between layers 2-3 and 3-4. This network acts on a flattened form of the input state and outputs a flattened state that is reshaped into a square matrix. We use the Adam optimiser with an initial learning rate of 10^{-4} and a scheduler that reduces this rate by a factor of 0.99 to a minimum of 10^{-9} when the loss stops decreasing. Where we have used data-specific parameter settings, these are given in Table 2.

[Redacted for anonymity]

Dataset	Parameter				
	batch size*	epochs	α	T	w
Planar	256	200	0.1	6	4096
SBM	256	20	1	15	1024
DCSBM	8	100	1	20	4096

Table 2. Choices of hyperparameters for G^3 . *: Batch size is the *maximum* batch size; for sets of graphs of different sizes, batches are formed by selecting only graphs of the *same* size, up to a maximum of `batch_size`.

D.2. Variable numbers of nodes

When dealing with sets of graphs with different numbers of nodes we can choose to deal with these in different ways. The most naïve approach is to simply pad adjacency matrices with zero rows and columns until all of them have $n = \max\{n_1, \dots, n_N\}$ “nodes”. Using this method, the heat kernel must be similarly padded to ensure matching dimensions.

Clearly, this is both inefficient and undesirable. Whilst padding can be helpful for simplicity, it can be more effective to (additionally) mask these zeros during training by defining suitable modifications to the MLP architecture to account for this. Specifically, we define a `MaskedLinear` module as a drop in replacement for the standard PyTorch `Linear` module in our neural architecture. The functionality of this is to take as an argument the number of nodes for a given input and index only the portion of the weight matrix up to the corresponding size of the (flattened) input state (i.e. $\frac{1}{2}n(n - 1)$).

Where datasets include graphs with disconnected nodes, we train only on the largest connected subgraph.

D.3. Architecture for Related Work

Due to hardware limitations, we were unable to run either the DeFoG model exactly as given in the configuration files supplied with it, or the SPECTRE model with the details given in the Readme file. Time constraints led us to reduce the number of epochs in the SPECTRE training from 6000 to 5000. Both time and memory constraints forced us to make the following changes to the DeFoG SBM configuration file (which was duplicated in the case of DCSBMs, there being no pre-specified configuration file in that instance):

Parameter	Original	Modified
batch size	32	8
epochs	50000	40000
layers	8	4
RRWP steps	20	10

Table 3. Table of modified parameter choices for the DeFoG SBM config. file.

The configuration file for planar graphs was left unchanged for DeFoG. We noted that, in spite of different training parameters being provided in the SPECTRE Readme file for planar graphs (vs SBMs), we obtained better performance with the SBM settings than we did with the planar settings. For the Enzymes dataset, for which neither SPECTRE nor DeFoG has recorded configurations, we adopted very similar parameter settings to those provided for the Proteins dataset, due to the relative similarity between the graphs in these two datasets. The only differences are as follows: for SPECTRE, we reduced the maximum number of training epochs from 1020 to 400 due to time constraints; for DeFoG, although dataset infrastructure was in place for Proteins, there was no configuration file. As such, we adopted the planar settings but with the epochs reduced from 100000 to 1000 for Proteins and 2000 for Enzymes.

DeFoG* and SPECTRE* In Section 5.5 we introduced DeFoG* and SPECTRE* as computationally limited forms of each model. Table 4 shows how we constrained relevant parameters to reduce computation time.

Model	Data	Original	Modified
SPECTRE*	Proteins	1020	10
SPECTRE*	Enzymes	400	4
DeFoG*	SBM	40000	1000
DeFoG*	DCSBM	40000	1000
DeFoG*	Planar	100000	1000

Table 4. Table of training epoch reductions for DeFoG* and SPECTRE* by dataset.

E. Framework Extensions

E.1. Asymmetric Heat Kernel

In Section 2 we consider the heat equation on a graph and define a *symmetric heat diffusion* that applies the heat kernel to the left and right of some graph matrix representation. We go on to outline the behaviour of this process and how it fits into the generator matching methodology.

In this section, we consider the more obvious *asymmetric* heat diffusion, where $Y_s := H_s Y_0$ (using the same notation as in Section 2) and provide an abridged summary of the corresponding quantities and modifications to G^3 , primarily through Table 5. Many of the asymmetric quantities are intuitive, however the choice of X_0 , which depends on the choice of matrix representation Y_0 , requires further explanation. For example, in the case of $Y_0 = A$, the standard adjacency matrix, we have a limit matrix of $\frac{1}{n} \mathbf{1} \mathbf{d}^\top$, where \mathbf{d} is the vector of degrees of A . From this, we could define a base distribution with elements $X_0 := \tilde{\mathbf{x}}_0 \mathbf{v}_0^\top$, where $\tilde{\mathbf{x}}_0 \sim \text{Dirichlet}(\alpha \mathbf{1})$ and $\log \mathbf{v}_0 \sim \mathcal{N}(\hat{\mu}_d, \hat{\sigma}_d^2)$ with $\hat{\mu}_d, \hat{\sigma}_d^2$ the logarithm of the mean and variance of the scaled degree vectors from the training set, i.e. $\hat{\mu}_d := \log(n^{-1} \langle \mathbf{d} \rangle)$. On the other hand, choosing $Y_0 = D^{-1} A$ (the

random walk matrix) leads to a limit matrix of $n^{-1}\mathbf{1}\mathbf{1}^\top$ and the natural choice of a pure Dirichlet base distribution, much like that described in the main text only without the symmetrisation and scaling.

Quantity	Symmetric	Asymmetric
$\mathcal{P}_s(Y)$	$H_s Y H_s$	$H_s Y$
$\frac{d}{dt} Y_t$	$-LY_t - Y_t L$	$-LY_t$
$\lim_{t \rightarrow \infty} Y_t$	$\frac{1}{n}(\mathbf{1}^\top Y_0 \mathbf{1})\mathbf{1}\mathbf{1}^\top$	$\frac{1}{n}\mathbf{1}\mathbf{1}^\top Y_0$
$X_0(A)$	$\langle d \rangle (\tilde{X}_0 + \tilde{X}_0^\top)$	$\tilde{\mathbf{x}}_0 \mathbf{v}_0^\top$

Table 5. Definitions of key quantities under the symmetric and asymmetric heat kernel processes.

E.2. Alternate Graph Representations and Heat Kernels

In Section 3.2–3.3 we describe the general scheme for heat kernel generator matching and sampling. To build a practical implementation of this scheme the user still has various choices to make. The most salient of these is the choice of matrix-representation of the graph, as this dictates a corresponding base distribution. As described in the preceding section, under symmetric and asymmetric formulations, a choice of $Y_0 = A$ leads to different samples X_0 . Other representations are possible, such as the random walk matrix $D^{-1}A$ or the symmetrised form $D^{-\frac{1}{2}}AD^{-\frac{1}{2}}$.

For simplicity, the main text focusses on the heat kernel formulation using the combinatorial Laplacian. However, it is straightforward to generalise the approach to other kernels, provided they satisfy suitable stochasticity properties. One alternative is the *random walk kernel*, which is shown to be a valid choice in Theorem E.1. If such an alternative is used, suitable limiting matrices and base distributions must be computed. In Table 6 we consider replacing the combinatorial Laplacian with the random walk and normalised Laplacians, $L_{rw} = I - D^{-1}A$ and $L_N = I - D^{-\frac{1}{2}}AD^{-\frac{1}{2}}$ as well as the random walk and lazy random walk kernels.

Lemma E.1. *The (lazy) random walk kernel is a valid probability transition kernel.*

Proof. Let $Q\Lambda Q^{-1}$ be the eigendecomposition of $D^{-1}A$. We have that $D^{-1}A\mathbf{1} = \mathbf{1}$, hence $\mathbf{1}$ is an eigenvector with eigenvalue 1. By eigenvector orthogonality we know that $Q^{-1}\mathbf{1} = c^{-1}\mathbf{e}_1$. Thus, $Q\Lambda^t Q^{-1}\mathbf{1} = Q\Lambda^t c^{-1}\mathbf{e}_1 = Q\lambda_1^t c^{-1}\mathbf{e}_1 = \mathbf{q}_1/c = \mathbf{1}$ since $\lambda_1 = 1$ and we have ordered the eigenvalues such that $\mathbf{q}_1 = Q_{:,1} = c\mathbf{1}$ is the first column vector of Q . The same argument applies in the case of the lazy random walk operator, $\frac{1}{2}(I + D^{-1}A)$. \square

The limiting form of the random walk matrix is given by $(D^{-1}A)^t \xrightarrow{t \rightarrow \infty} Q J^{11} Q^{-1}$, where J^{ij} is the matrix of zeros with a single 1 at the ij th entry. This simplifies to the rank-1 matrix $\mathbf{q}_1 \mathbf{q}_1^{-\top}$, where $\mathbf{q}_1^{-\top}$ is the 1st row of Q^{-1} which further simplifies to $c\mathbf{1}\mathbf{q}_1^{-\top}$, since the first eigenvector is a constant multiple of the vector of ones. The same argument applies to the lazy random walk matrix. In practice this quantity tends to be close to the heat limit anyway; the perturbation comes from the lack of symmetry of the random walk matrix, which can be quantified by the commutator $[D^{-1}, A] = D^{-1}A - AD^{-1}$.

Kernel	Valid	Limit
e^{-tL}	✓	$n^{-1}\mathbf{1}\mathbf{1}^\top$
$e^{-tL_{rw}}$	✓	$n^{-1}\mathbf{1}\mathbf{1}^\top$
e^{-tL_N}	✗	$n^{-1}\mathbf{1}\mathbf{1}^\top$
$(D^{-1}A)^t$	✓	$q_{11}\mathbf{1}\mathbf{q}_1^{-\top}$
$\frac{1}{2^t}(I + D^{-1}A)^t$	✓	$q_{11}\mathbf{1}\mathbf{q}_1^{-\top}$

Table 6. Validity of probabilistic interpretation and limiting behaviour for different kernels.

Further, any such kernel can be symmetrised to act on both the right and left of the subject matrix as is described in the main text for the heat kernel.

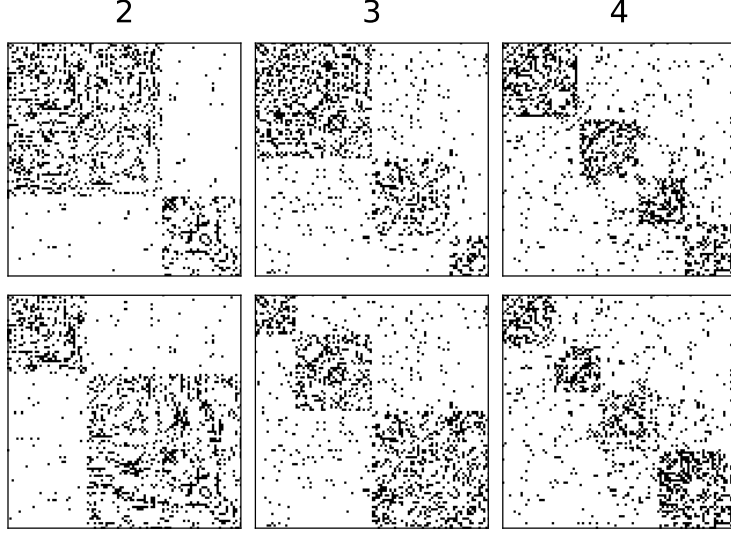


Figure 4. SBM adjacency matrices generated by pre-specifying node labels to the conditional form of the G^3 model. Columns headers indicate the number of communities and the top row uses a given ratio of membership sizes with the bottom row using the sizes reversed in order.

E.3. Conditional Graph Generation

Another choice of matrix representation leads to a bonus formulation that provides a natural way to include covariate information for the purposes of conditional generation (often known as “guidance” in the generative literature). Covariate-assisted spectral clustering (Binkiewicz et al., 2017) uses node-level covariate information to aid spectral-based clustering techniques. The key to the approach is to augment the Laplacian in the following way: $L_\omega := L + \omega ZZ^\top$ for some tuning parameter ω and covariates Z . We adopt this augmentation for our matrix representation (Y_0) and observe that, for vector-valued Z (denoted \mathbf{z}), $\lim_{t \rightarrow \infty} H_t L_\omega = n^{-1} \omega \mathbf{1} (\mathbf{1}^\top \mathbf{z}) \mathbf{z}^\top$; in other words, the limiting distribution depends *explicitly* on the node covariates. This leads to a natural way to implement graph generation conditioned on pre-specified covariate information by constructing suitable limit matrices analogously to those described in Section E.2.

In Figure 4, we demonstrate evidence of this approach in action on a toy example of SBM generation. In each column of the figure we generate different numbers of communities, with pre-chosen membership ratios: this information is encoded directly into vectors $(\mathbf{z}_i)_{i=1}^{N^*}$ for N^* new graphs and used to construct matrices of the form $X_0 = n^{-1} \hat{\omega} (\tilde{\mathbf{x}}_0^\top \mathbf{z}) \tilde{\mathbf{x}}_0 \mathbf{z}^\top$ for $\tilde{\mathbf{x}}_0 \sim \text{Dirichlet}(\alpha \mathbf{1})$.

F. Additional Experimental Results

In this section we include figures indicating the behaviour of G^3 with respect to training (and sampling) variables, including the number of graphs, number of nodes and choice of α parameter for the base distribution.

Figure 5a shows spectral MMD as a function of T and the number of nodes in the graphs. Perhaps surprisingly, the apparent minima of the curves seems to occur at approximately the same T which perhaps indicates that N is the more important factor. The curves also appear to suggest that the problem gets “harder” as n increases, at least for the planar graphs shown here.

Figure 7 supplements Figure 2 and Figure 5a by showing how the proportion of non-unique output graphs depends on n and N (and T). Roughly, the spectral performance and non-uniqueness have some negative correlation, indicating that care needs to be taken to optimise overall quality of graph output.

Table 7. Median (\pm median abs. deviation) of MMD metrics for G^3 , DeFoG*, SPECTRE* over 3 – 5 randomly seeded splits. Lower is better and **bold** indicates best performance, based on the median plus one median abs. deviation. Training-test set comparisons are also included to show best possible performance.

Dataset	Model	Clustering	Degree	Orbit	Spectrum	Triangles
SBM	G^3	0.0356 ± 0.0005	0.0318 ± 0.0052	0.0631 ± 0.0120	0.0796 ± 0.0120	0.0270 ± 0.0078
	Asymm. G^3	0.0398 ± 0.0010	0.0390 ± 0.0052	0.0710 ± 0.0140	0.0832 ± 0.0015	0.0287 ± 0.0084
	DeFoG*	0.0513 ± 0.0005	0.6270 ± 0.0027	0.0500 ± 0.0000	1.6600 ± 0.0003	0.0818 ± 0.0030
	Training	0.0312 ± 0.0000	0.0028 ± 0.0013	0.0312 ± 0.0000	0.0055 ± 0.0004	0.0017 ± 0.0002
DCSBM	G^3	0.1270 ± 0.0091	0.0344 ± 0.0062	0.0971 ± 0.0057	0.1230 ± 0.0330	0.0110 ± 0.0098
	Asymm. G^3	0.2340 ± 0.0160	0.0810 ± 0.0200	0.1420 ± 0.0170	0.1010 ± 0.0220	0.0578 ± 0.0250
	DeFoG*	0.1110 ± 0.0056	0.7370 ± 0.0015	0.0665 ± 0.0003	1.2600 ± 0.0041	0.4330 ± 0.0210
	Training	0.0291 ± 0.0009	0.0017 ± 0.0007	0.0286 ± 0.0025	0.0277 ± 0.0069	0.0012 ± 0.0002
Planar	G^3	0.3090 ± 0.0300	0.0030 ± 0.0015	0.0035 ± 0.0018	0.0060 ± 0.0015	0.0467 ± 0.0360
	Asymm. G^3	1.0200 ± 0.0440	0.0074 ± 0.0050	0.0106 ± 0.0089	0.0113 ± 0.0021	0.1110 ± 0.0320
	DeFoG*	0.1200 ± 0.0043	0.7350 ± 0.0010	1.0100 ± 0.0014	1.9500 ± 0.0160	0.0296 ± 0.0005
	Training	0.0224 ± 0.0021	0.0004 ± 0.0000	0.0002 ± 0.0001	0.0004 ± 0.0002	0.0050 ± 0.0016
Enzymes	G^3	0.0225 ± 0.0008	0.0854 ± 0.0550	0.0902 ± 0.0390	0.0755 ± 0.0220	0.0490 ± 0.0380
	Asymm. G^3	0.0803 ± 0.0200	0.0934 ± 0.0520	0.1040 ± 0.0047	0.1090 ± 0.0480	0.0752 ± 0.0120
	SPECTRE*	0.0598 ± 0.0110	0.7290 ± 0.0043	0.6140 ± 0.0230	1.1700 ± 0.0590	0.4700 ± 0.0096
	Training	0.0122 ± 0.0002	0.0004 ± 0.0004	0.0024 ± 0.0014	0.0114 ± 0.0024	0.0021 ± 0.0001
Proteins	G^3	0.0465 ± 0.0009	0.0220 ± 0.0012	0.5530 ± 0.0720	0.1600 ± 0.0074	0.0928 ± 0.0180
	Asymm. G^3	0.0750 ± 0.0073	0.0345 ± 0.0003	0.3480 ± 0.2000	0.0921 ± 0.0110	0.0419 ± 0.0071
	SPECTRE*	0.1070 ± 0.0000	0.3600 ± 0.0650	0.7820 ± 0.0250	0.3750 ± 0.0044	0.0358 ± 0.0240
	Training	0.0504 ± 0.0001	0.0012 ± 0.0001	0.0093 ± 0.0010	0.0568 ± 0.0003	0.0011 ± 0.0003

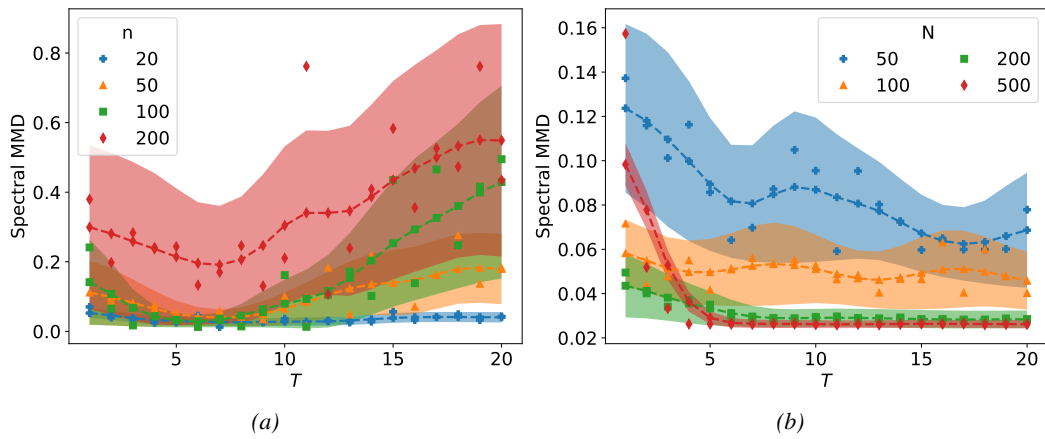
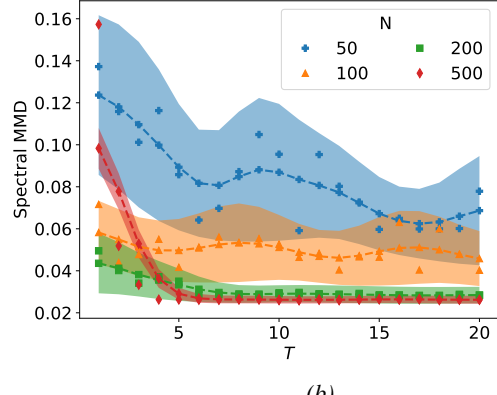


Figure 5. Spectral MMD as a function of T and number of nodes, n , for $(N = 100)$ (a) planar graphs and (b) SBMs. Curves are Gaussian-smoothed¹ functions of the observations shown, which themselves are averaged over 10 random seeds. Shaded regions indicate 66% confidence intervals under CLT assumptions. Learning rate set at 1×10^{-4} for training.

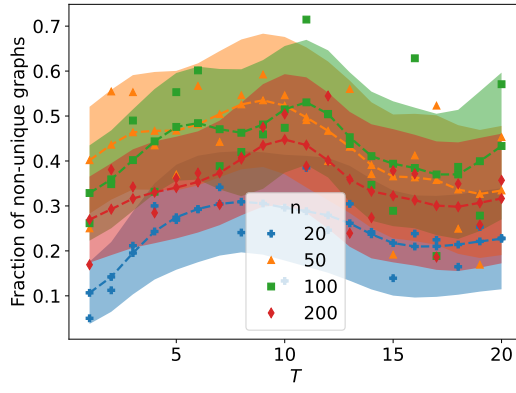
N	T	spec	
		w	$1024 \quad 0.020 \pm 0.019$
100	15	2048	0.027 ± 0.022
		4096	0.041 ± 0.043

(a)

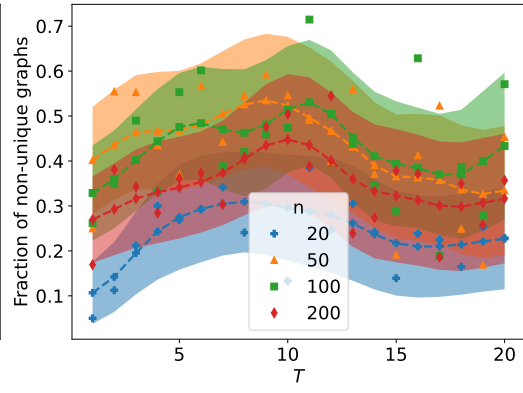


(b)

Figure 6. (a) Spectral MMD for different choices of w , the number of hidden nodes per layer, for fixed T and N (for SBMs). (b): Spectral MMD as a function of T and number of graphs N for SBMs. Curves are Gaussian-smoothed¹ functions of the observations shown, which themselves are averaged over 10 random seeds. Shaded regions indicate 66% confidence intervals under CLT assumptions. Learning rate set at 1×10^{-4} for training.



(a)



(b)

Figure 7. Proportion of non-unique generated graphs, as a function of T . (a): Planar graphs ($n = 64$) for different sizes of dataset, N . (b): Planar graphs ($N = 100$) for different sized graphs. Curves are Gaussian-smoothed¹ functions of the observations shown, which themselves are averaged over 10 random seeds. Shaded regions indicate 66% confidence intervals under CLT assumptions. Learning rate set at 1×10^{-4} for training.

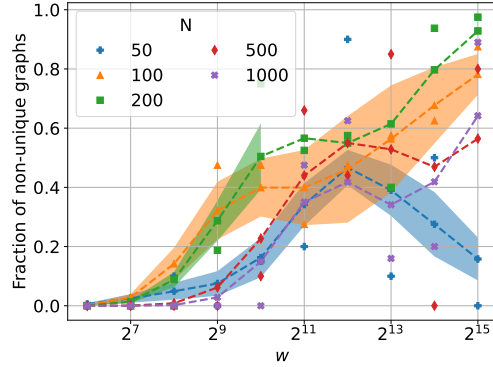


Figure 8. Proportion of non-unique generated planar graphs as a function of w , the number of nodes per hidden layer, and number of graphs N . Curves are Gaussian-smoothed¹ functions of the observations shown, which themselves are averaged over 10 random seeds. Shaded regions indicate 66% confidence intervals under CLT assumptions. Learning rate set at 1×10^{-4} for training.

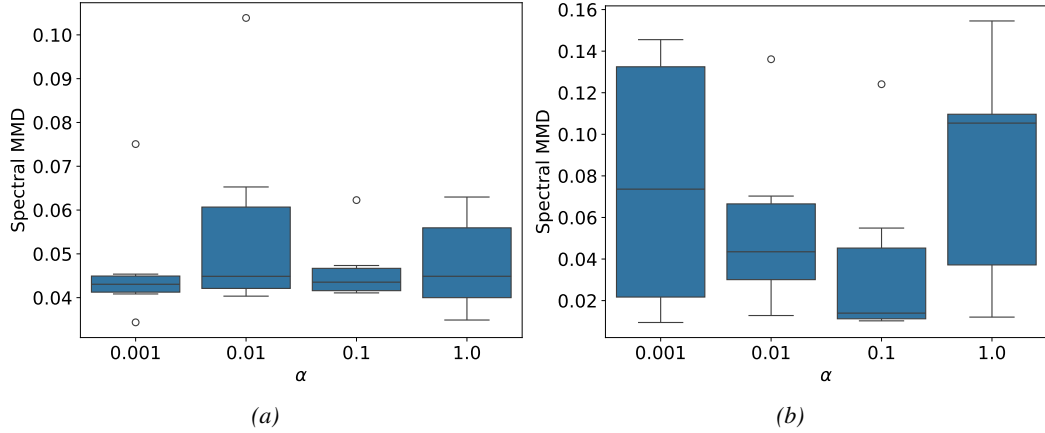


Figure 9. Spectral MMD as a function of α , the Dirichlet concentration parameter for the base distribution. (a): results for 200-node SBM graphs; (b): results for 64-node planar graphs.

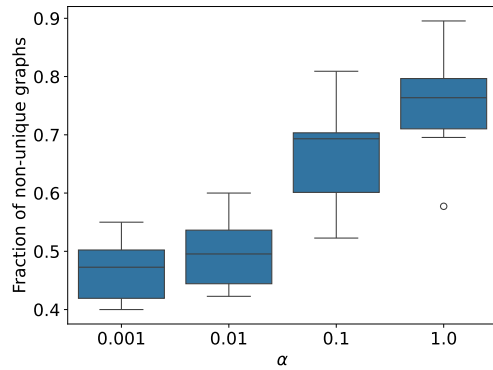


Figure 10. Fraction of (planar) graphs generated that are non-unique as a function of α .

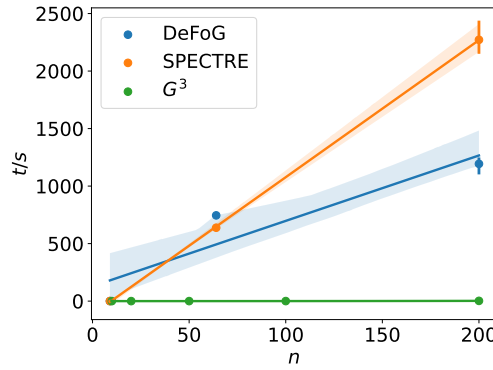


Figure 11. Training plus generation time per sample graph for DeFoG, SPECTRE, and G^3 .

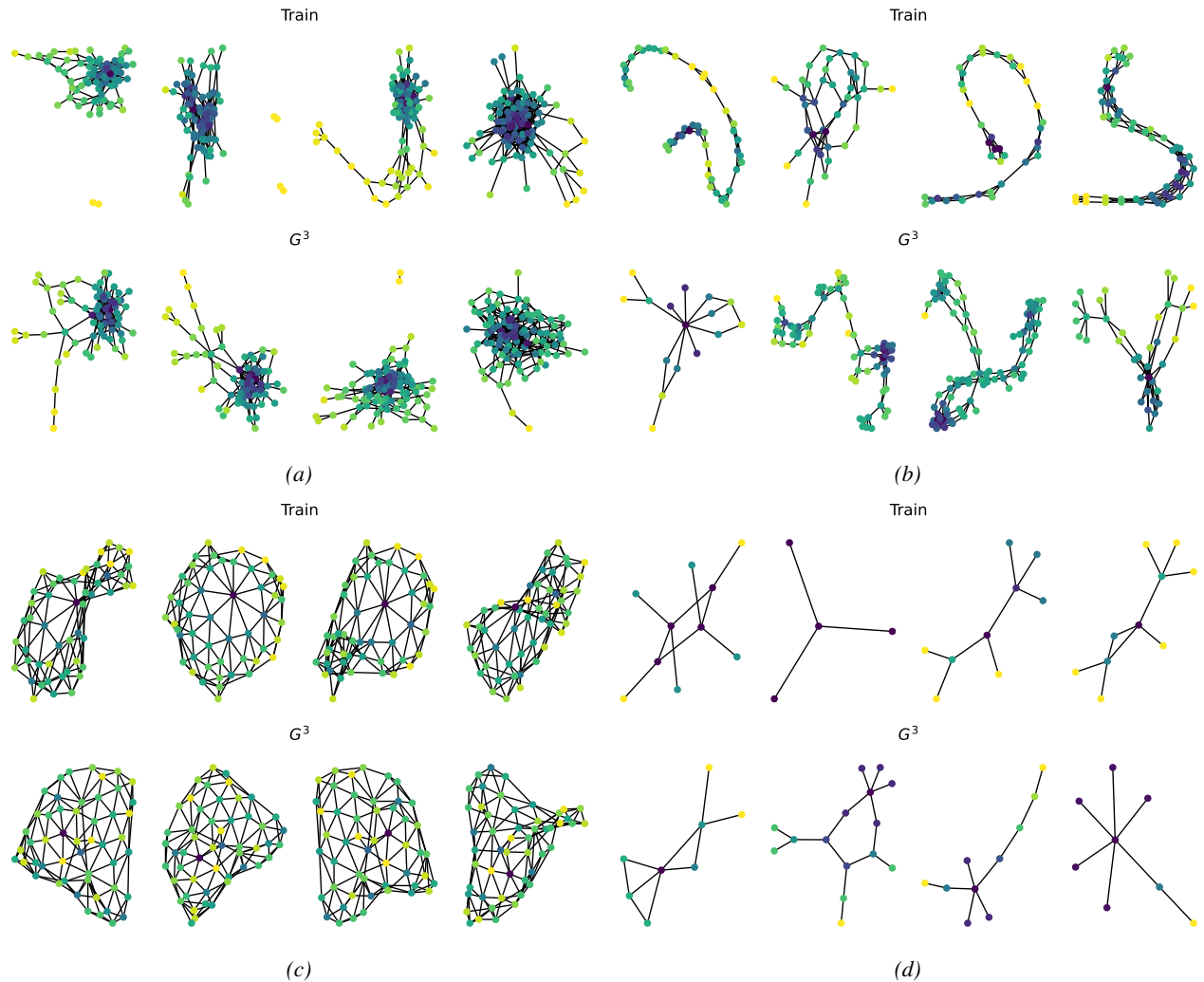


Figure 12. A series of example graphs drawn at random from a training set (top) and the output of G^3 (bottom). (a): DCSBM, (b): Protein, (c): Planar, (d): QM9. Node colouring reflects Forman-Ricci curvature at that node.

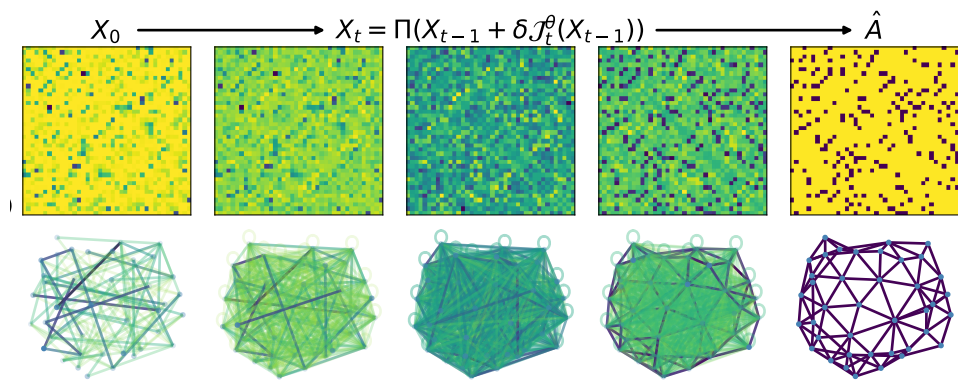


Figure 13. Example reconstruction of a graph from a sample from the base distribution.